On the Accuracy of Physics- and Correlation-Based Turbulence Models at Low Reynolds Numbers

Prateek Ranjan[1], Wesley H. Warton [2] and Kai A. James [3]
University of Illinois at Urbana-Champaign, Urbana, Illinois 61801

The three-dimensional Unsteady Reynolds-Averaged Navier-Stokes (URANS) $k-\omega-SSTLM$ and $k_T-k_L-\omega$ turbulence models were studied to understand their application and transition prediction capability for in-compressible flow regimes. Additionally, we present a novel protocol for systematically studying the near-wall flow physics over a sharp trailing edged SD7003 airfoil, subjected to flow with varying free-stream intensities and angles of attack, at three chord-based Reynolds numbers: 6×10^4, 6×10^5, 6×10^6. Complex low-Reynolds number near-wall flow phenomenon known as the formation and destruction of the Laminar Separation Bubble, eventually leading to flow transition from the laminar to the turbulent regime was resolved using both turbulence models, and their accuracy was compared with Implicit Large Eddy Simulation surface pressure predictions. Mean and instantaneous flow-fields were extracted, thus leading to a more thorough quantitative and qualitative comparison. Considering all flow characteristics, the correlation based $k-\omega-SSTLM$ turbulence model was shown to predict more reasonable flow transition characteristics for simple airfoil configurations. easily ~~**Hellow world**~~

---

[1] Graduate Research Assistant, Department of Aerospace Engineering
[2] Undergraduate Research Assistant, Department of Aerospace Engineering,
[3] Assistant Professor, Department of Aerospace Engineering, Member AIAA

Nomenclature

c = airfoil chord

C_d = sectional drag coefficient

C_l = sectional lift coefficient

D = Drag

L = Lift

k = kinetic energy

k_L = laminar kinetic energy

k_T = turbulent kinetic energy

ω = specific dissipation rate

R_p = reattachment point

Re_c = chord-based Reynolds number

Re_θ = momentum thickness Reynolds number

$Re_{\theta t}$ = transition-onset momentum thickness Reynolds number

Re_ν = vorticity Reynolds number

s = first layer cell height

S = absolute value of strain rate

S_p = separation point

Tu_∞ = free-stream turbulence intensity

T_p = transition-onset point

U = free-stream velocity

α = angle of attack

η = horizontal computational plane

μ = dynamic viscosity

ν = kinematic viscosity

ρ = free-stream density

σ = strain rate

θ = boundary layer thickness

ξ = vertical computational plane

I. Introduction and Motivation

Design of highly efficient wing configurations for both sub and supersonic flight regimes has been a tedious and never-ending quest for aircraft aerodynamicists all over the globe, since before the first human powered flight [1]. The quest for more fuel efficient flight requires the basic but critical performance characteristics such as low induced and profile drag along with structural design considerations such as weight and wing root bending moment. Although the current state of the art in wing design in primarily focused towards transonic and supersonic flight regimes, design of low speed lifting surfaces such as the case of sailplanes and small transport wings are of key importance, particularly from a pure aerodynamics perspective. Considering the recent interest of the logistics sector in UAVs [2–6], design of long-range and high performance wing configurations has never been more important. Similar to such long range UAV systems, the sailplane design community, over the past few decades, has slowly progressed towards a new class of wings, designed using multi-disciplinary approach for high overall L/D over multiple flight regimes [7, 8]. A key commonality between the UAV and sailplane wing configurations is their operating flight Reynolds number in the range of $10^4 - 10^6$ [8, 9]. Near-wall effects in the stated Reynolds number range are often characterized by strong adverse pressure gradients, thus giving rise to boundary layer instabilities and separation in the laminar region. More commonly termed as the laminar separation bubble (LSB), it is one of the dominant boundary layer phenomenon that dictate aerodynamic performance at low speeds. A comprehensive analysis on the structure and external factors that lead to LSB formation and bursting is widely reported in the literature [10–14]. Hence, the design of UAV and sailplane wing configurations must involve the key critical aspect of the LSB and its effect on performance of the lifting surface during flight.

At the design stage, studies in the past have reported the use of inviscid potential flow based analysis tools, in addition to the relatively newer integral boundary layer potential flow methods [8, 15]. Though such low fidelity tools are highly efficient choices for aerodynamic analysis at high Reynolds numbers, their capability to model flow transition mainly depends on linear stability theory [16, 17], which as reported in a recent study by Counsil *et al.* [15], generally under-predicts the effect of LSB on the aerodynamic characteristics. High fidelity URANS based approaches are a

more appealing choice to resolve such effects, however, such an approach is often computationally expensive. Due to such high computational costs, the use of high fidelity analysis methods in a large airfoil optimization framework is often deemed inefficient [18, 19]. A relatively new design methodology wherein the low-fidelity potential flow model is used for preliminary design analysis followed by a high fidelity Navier-Stokes simulation has been reported by Ranjan *et al.* [20] and Ranjan *et al.* [21].

The use of URANS based Navier-Stokes simulations to resolve LSB characteristics is not new and is extensively reported in the open literature. Early works of Howard *et al.* [22] and Benton *et al.* [23] in addition to other studies [24–26] to investigate flow transition over a flat plate , often serve as the foundation to the current methods in turbulence modeling to resolve flow transition. Models such as those proposed by Wilcox [27], have performed well for simple configurations but are less reliable for complex surfaces, especially when the transition point is not known apriori. Though there exists an abundance of turbulence models written especially for modeling laminar-turbulent flow transition, a few such as the two-layer model by Menter [28], the Reynolds stress model of Wilcox [27] and Wallin *et al.* [28] have been shown to predict aerodynamic drag and lift to a reasonable accuracy within the URANS framework. In addition to such high fidelity URANS approaches for resolving near-wall effects of flow transition, Large Eddy Simulation (hereafter LES) has also been widely used and reported in the open literature. One such example, relevant to the nature of the current study is a study by Galbraith *et al.* [30] wherein computations for the entire drag polar for a SD 7003 airfoil at Re 6×10^6 have been reported. Though such high order simulations are often used as a reference to validate the URANS results [31], one might argue there is an over-estimation of drag reported in [30].

The goal of the current study is to compare two URANS-based turbulence closure models, widely used for LSB bound flow regimes. Comprehensive comparisons are drawn between the four equation $k - \omega SSTLM$ or more commonly known as the $\gamma - Re_\theta$ turbulence model [32], and the Eddy-viscosity based $k_T - k_L - \omega$ turbulence model [33]. While a large number of studies in the past have been based on the validation and application of the former, only a handful of studies in the recent past have addressed the application of the latter [34–36]. The study of near-wall fluid

physics of these airfoils is not new and has been widely reported in the literature [15, 31, 37–40], especially for the SD7003 airfoil given its superior performance due to a long and stable LSB at low Reynolds numbers [37, 41]. However, per the authors current knowledge, a quantitative comparison of the two previously stated turbulence models is missing in the literature. The importance of such a comprehensive comparison between the two turbulence models was first felt necessary during the design and analysis stages in [20, 21]. In order to draw quantitative and qualitative comparisons between the two turbulence closure models, both instantaneous and time-averaged analyses are performed in an URANS computational framework. In order to obtain a comprehensive comparison of the two models, we have developed a novel framework to systematically evaluate the sensitivity of near-wall flow physics especially attributes such as separation point (S_p), transition point (T_p) and re-attachment point (R_p), on flow angle of attack, free stream turbulence intensities and chord-based Reynolds number.

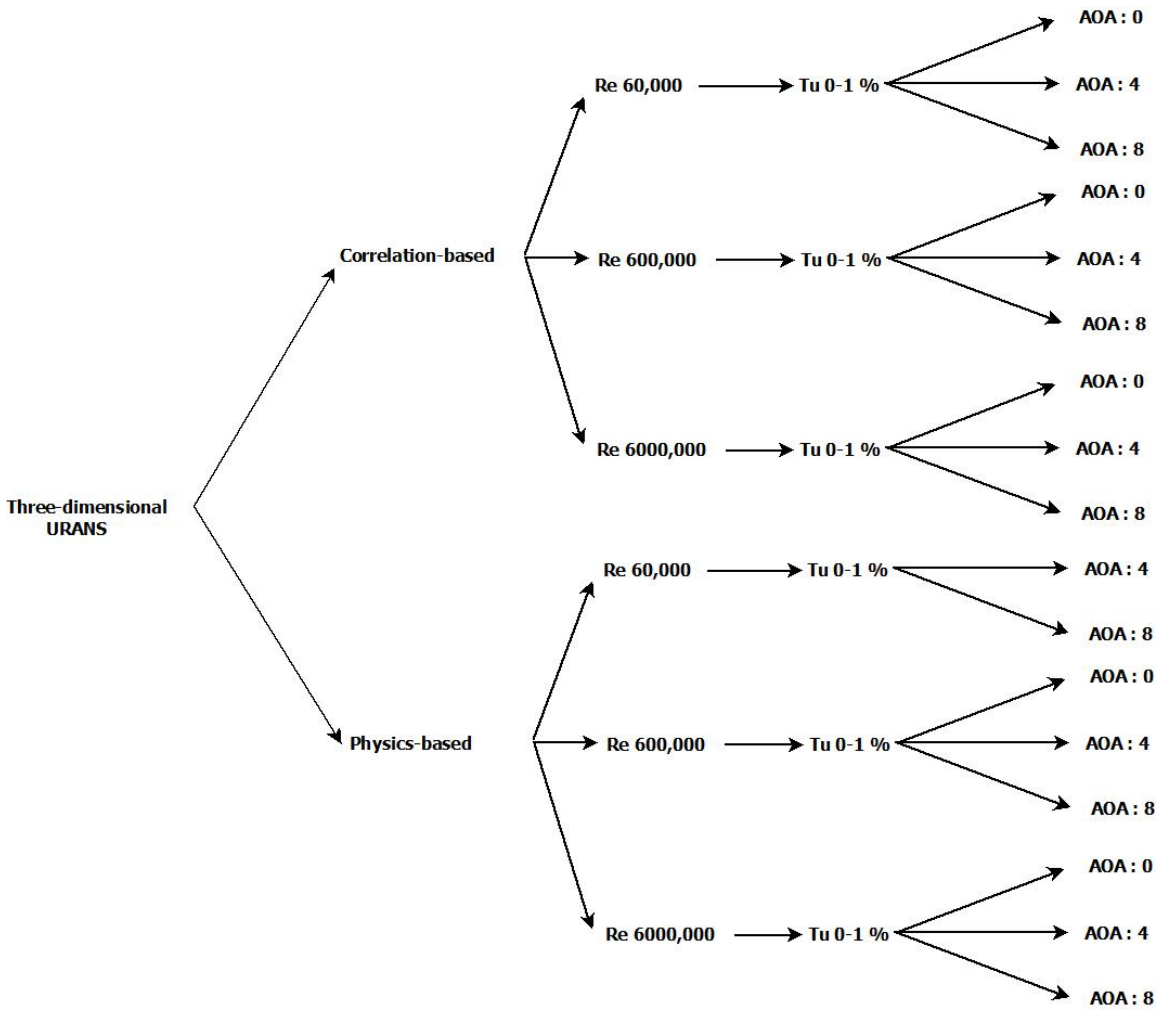

Fig. 1: Evaluation protocol schematics

II. Computational framework

An open-source, three-dimensional computational fluid dynamics package by Weller *et al.* [42] was used as the numerical platform to study the application of the two turbulence models. Based on a monolithic, object oriented structure in $C++$, it allows for easy compilation and modification of existing libraries. This allows for better understanding of the underlying source code as compared to other CFD toolkits written in procedural languages [42, 43]. The application and accuracy of the flow solver has been the object of numerous studies [44–48] and recent wing design studies such as [20] and [21]. While the mathematical framework encompassing these turbulence models may be universal, the approach in their application may differ from one numerical platform to another.

The $k-\omega-SSTLM$ model [28] is a four-equation turbulence model based on the transition-

onset Reynolds number, $Re_\theta t$ which in turn is a function of the maximum strain-rate Reynolds number, expressed as [28]:

$$Re_\theta = \frac{max(Re_v)}{2.193}, \tag{1}$$

where,

$$Re_v = \frac{y^2 s}{\nu} \tag{2}$$

Here s is the strain rate magnitude which is computed at each grid point in the computational domain and y is the length function, thus making the turbulence model based on local a property of the flow. The transport equations for the model are described in detail in [27]:

$$\frac{\partial(\rho k)}{\partial t} + \frac{\partial(\rho U_j k)}{\partial x_j} = \tilde{P}_k - beta^* \rho k\omega + \frac{\partial}{\partial x_j}\left[(\mu + \sigma_k \mu_t)\frac{\partial k}{\partial x_j}\right] \tag{3}$$

$$\frac{\partial(\rho\omega)}{\partial t} + \frac{\partial(\rho U_j \omega)}{\partial x_j} = \alpha\rho S^2 - \beta\rho\omega^2 + \frac{\partial}{\partial x_j}\left[(\mu + \sigma_\omega \mu_t)\frac{\partial \omega}{\partial x_j}\right] + 2(1 - F_1)\rho\sigma_{\omega 2}\frac{1}{\omega}\frac{\partial k}{\partial x_j}\frac{\partial \omega}{\partial x_j} \tag{4}$$

$$\frac{\partial(\rho\gamma)}{\partial t} + \frac{\partial(\rho U_j \gamma)}{\partial x_j} = P_\gamma - E_\gamma + \frac{\partial}{\partial x_j}\left[\left(\mu + \frac{\mu_t}{\sigma_\gamma}\right)\frac{\partial \gamma}{\partial x_j}\right] \tag{5}$$

$$\frac{\partial(\rho\tilde{Re}_{\theta t})}{\partial t} + \frac{\partial(\rho U_j \tilde{Re}_{\theta t})}{\partial x_j} = P_{\theta t} + \frac{\partial}{\partial x_j}\left[\sigma_{\theta t}(\mu + \mu_t)\frac{\partial \tilde{Re}_{\theta t}}{\partial x_j}\right] \tag{6}$$

Equations. 3 and 4 correspond to transport equations of the baseline SST model by Menter *et al.* [26]. The latter two transport equations are an addition to those from the SST model transport equations. Equation 5 is implemented for the intermittency which triggers the onset of the transition when $\gamma > 0$. On the other hand , Eq. 6 corresponds to the transition momentum-thickness Reynolds number (Eq. 1) which in turn indicates the location in the near wall region of the computational domain where onset occurs, and resolves the effect of the free stream turbulence intensity, Tu_∞, and pressure gradient on the boundary layer-near field interface. In Eq. 5, P_γ and E_γ are the source

terms. For instance, E_γ is zero in the laminar flow regime and non-zero whenever the local strain-rate Reynolds number becomes greater than the local transition-onset condition. Equation 6 enables an empirical correlation approach to compute the momentum-thickness-based Reynolds number in the far-field and allow for diffusion into the shear layer. The transport equations for momentum-thickness Reynolds number and intermittency are coupled with the SST transport equations (Eq. 3 and Eq .4) with an additional transport production term $\tilde{P_k}$ in Eq. 1 which is a function of γ. A detailed numerical description of the SSTLM turbulence model can be found in [27].

The $k_T - k_L - \omega$ turbulence model is an eddy-viscosity turbulence model based on the $k - \omega$ framework [33]. In addition to the transport equations of the baseline $k - \omega$ turbulence model, a third equation is introduced to resolve the low-frequency velocity fluctuations in the pre-transition region, which are often said to be the precursors to flow transition. In addition to the linear eddy-viscosity model for a single phase, steady flow, additional transport equations are solved for the k_T, k_L and ω, where ω is defined in terms of isotropic dissipation ϵ, as $\omega = \epsilon/k_T$. The additional transport equations are expressed as [33]:

$$\frac{Dk_T}{Dt} = P_{k_T} + R_{NAT} - \omega k_T - D_T + \frac{\partial}{\partial x_j}\left[\left(\nu + \frac{\alpha_T}{\sigma_k}\frac{\partial k_T}{\partial x_j}\right)\right] \tag{7}$$

$$\frac{Dk_L}{Dt} = P_{k_L} + R_{BP} - D_L + \frac{\partial}{\partial x_j}\left[\nu\frac{\partial k_L}{\partial x_j}\right] \tag{8}$$

$$\frac{D\omega}{Dt} = C_{\omega 1}\frac{\omega}{k_T}P_{k_T} + \left(\frac{C_{\omega E}}{f_W} - 1\right)\frac{\omega}{k_T}(R_{BP}+R_{NAT}) - C_{\omega 2}\omega^2 C_{\omega 3} f_\omega \alpha_T f_W^2 \frac{\sqrt{k_T}}{d^3} + \frac{\partial}{\partial x_j}\left[\left(\nu + \frac{\alpha_T}{\sigma_\omega}\right)\frac{\partial \omega}{\partial x_j}\right] \tag{9}$$

where the terms in Eq. 7, 8 and 9 consist of various production and destruction terms and ω is the inverse length scale. In Eq. 9, the first, third and fifth terms correspond to the turbulent production, destruction and gradient transport terms, analogous to the similar terms in the baseline $k - \omega$ framework [28]. A more complete definition of total fluctuation energy, production and destruction terms for the $k_T - k_L - \omega$ turbulence model can be found in [32]. The native distribution of the $k - \omega - SSTLM$ turbulence model was used for the current study. However, necessary corrections

in strain rate formulation for the physics-based $k_T - k_L - \omega$ turbulence model as recommended by Furst [49], were made.

A three-dimensional structured computational domain in a C-grid mesh topology was used for the SD7003 airfoil. The inlet was placed at a distance of $10c$ from the airfoil leading edge while the upper and lower far-field patches were placed at a distance of $20c$, and the outlet at a distance of $50c$. A structured mesh with C-topology allows for better control on the near-wall mesh attributes such as cell non-orthogonality, aspect ratio and skewness. In addition to such parameters,a wake baffle to resolve viscous wake and hence the corresponding induced effects are easy to implement in a C-grid. Moreover, a C-grid allows for far-field boundary conditions such as conventional inlet and outlet which are analogous to a typical wind tunnel setup. The structured Cartesian mesh was generated using a multi-block grid generation utility called $blockMesh$, native to the CFD framework. A blockMesh dictionary file generator script was written in $MATLAB$ [50] in order to achieve better control over mesh metrics such as cell aspect ratio, skewness and non-orthogonality of cells especially in the leading and trailing edge regions. To determine the correct mesh resolution considering a balance between solution accuracy and computational expense, the cell growth ratio (ΔS) in the $\eta - \xi$ plane was varied, while the spanwise cell density was kept constant, an approach similar to that used in Ranjan *et. al* [21]. A grid convergence study was conducted wherein four different mesh configurations were studied using both turbulence models. Fig. 3 represents the grid convergence characteristics using both $k_T - k_L - \omega$ (hereafter physics-based) and $k - \omega - SSTLM$ turbulence models for the SD7003 airfoil subjected to flow at Re 6×10^4 and $\alpha = 4^0$. Fig. 2 illustrates the leading and trailing edge characteristics for the four mesh configurations with increasing mesh density in the near-wall region. Figure 3 represents the grid convergence trends for time-averaged C_p distribution. While all mesh configurations predict the suction peak within reasonable accuracy when compared to the experiment, only meshes $C3$ and $C4$ resolve the laminar separation bubble to an agreeable extent. Greater degree of flow separation is observed for the relatively coarser mesh configurations. Interestingly, Fig. 3(b) indicates a more accurate solution from the $C4$ mesh configuration, as seen from the attached flow in the turbulent flow regime.

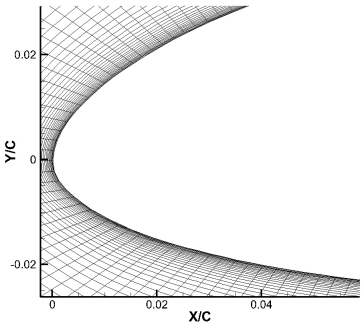

(a) $C1 : LE$

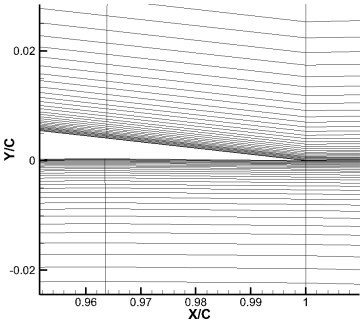

(b) $C1 : TE$

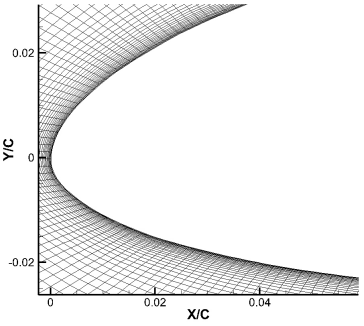

(c) $C2 : LE$

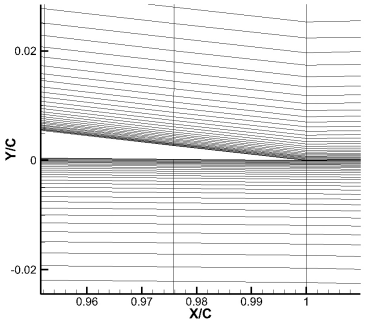

(d) $C2 : TE$

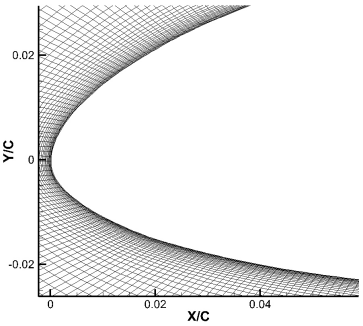

(e) $C3 : LE$

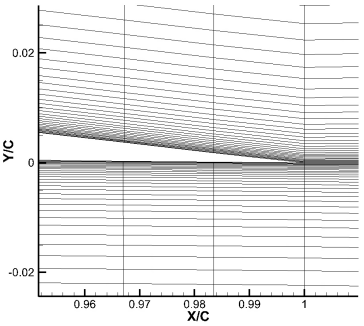

(f) $C3 : TE$

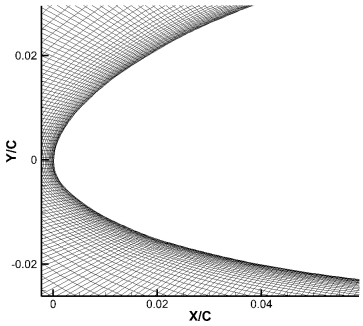

(g) $C4 : LE$

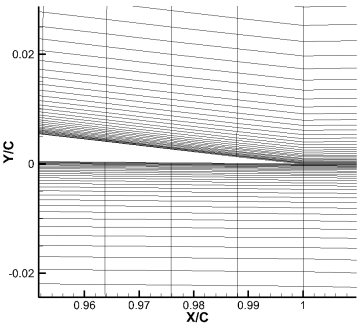

(h) $C4 : TE$

Fig. 2: Leading and trailing edge mesh resolution for C1 mesh configuration

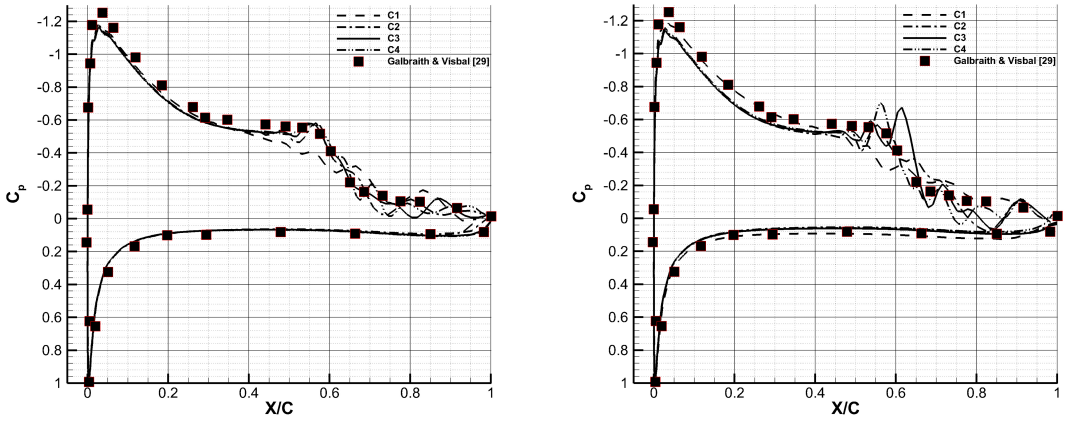

(a) $K_l - K_t - \omega$ (b) $K - \omega$ SSTLM

Fig. 3: URANS grid convergence characteristics for SD 7003 airfoil at Re 6×10^4, $\alpha = 4^0$

In the current study, all simulations were performed using an adjustable large-time-step transient solver, compiled within the OpenFOAM framework. Since for low-moderate Reynolds number the solver allows for an adjustable time-step or Courant number for a fixed mesh resolution, a separate convergence study for the $C3$ and $C4$ mesh configurations for the physics and correlation-based turbulence models, respectively, were performed to assess the solution stability and accuracy. One key motivating factor to perform such a parametric analysis was to choose the optimal Courant number for all the simulations such that the computational time was minimized while resolving the unsteady effects in the flow field as well as overall solution accuracy. Table 1 lists the Courant numbers used for the convergence study.

Case	Courant number
Case A	0.9
Case B	2
Case C	4
Case D	6
Case E	8
Case F	10
Case G	12
Case H	14

Table 1: Courant numbers used for parametric study

Fig. 4 represents the C_p distribution obtained from simulations at multiple Courant numbers. As observed from Fig. 4(b), the Case A exhibits the strongest agreement with the ILES data of Gablirath *et. al* [30]. With an increase in the Courant number, while the separation point remains less affected, the transition point as well as re-attachment point are vastly under-predicted. For instance, cases B, C and E over-predict the transition location whereas cases G and H suggest relatively upstream reattachment points, thus suggesting a smaller bubble size. In addition to such effects, with an increase in Courant number, the LSB is observed to disintegrate into smaller separation bubbles downstream of the transition point. For case A, the C_p distribution is observed to be in reasonable agreement with reference data of Gablirath *et. al* [30]. Although the separation, transition and reattachment points are reasonably resolved, the flow downstream of the reattachment point is appears to be detached. Similar observations were made by Counsil *et. al* [15] in their URANS study for a NACA 0012 airfoil. Another key observation made from Fig.4(a) is the increase in under-prediction of the suction peak as the Courant number increases. This loss of accuracy may be attributed to the increase in simulation time-step with for a fixed mesh size, thus resulting in loss of information in the transient domain.

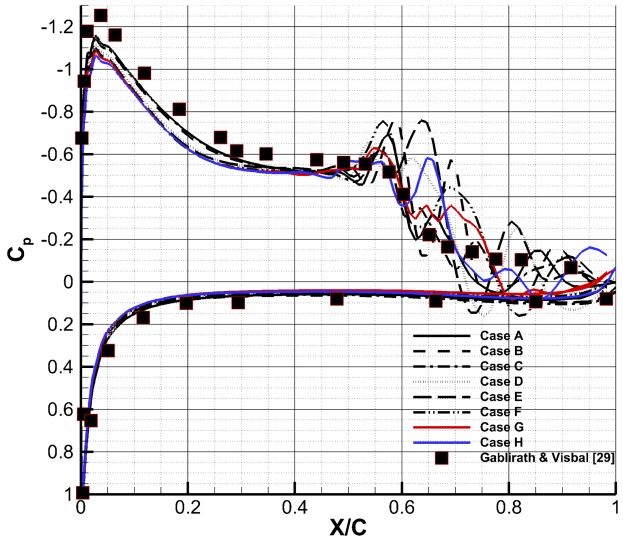

(a) $k_T - k_L - \omega$

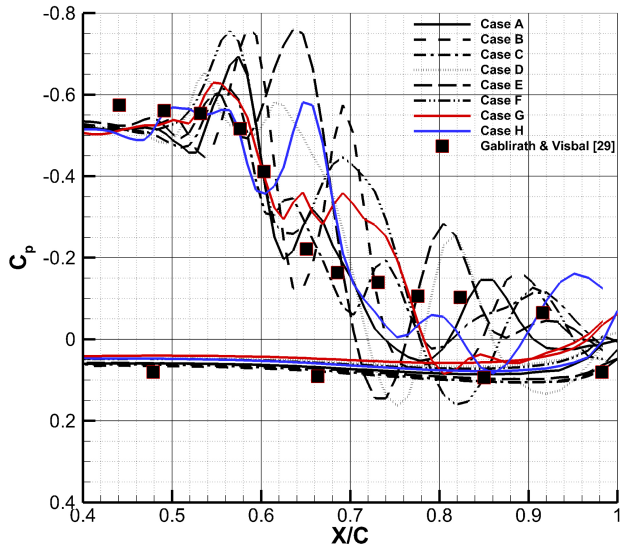

(b) $k - \omega - SSTLM$

Fig. 4: URANS grid convergence characteristics for SD 7003 airfoil at Re 6×10^6, $\alpha = 4^0$, for multiple Courant number simulations

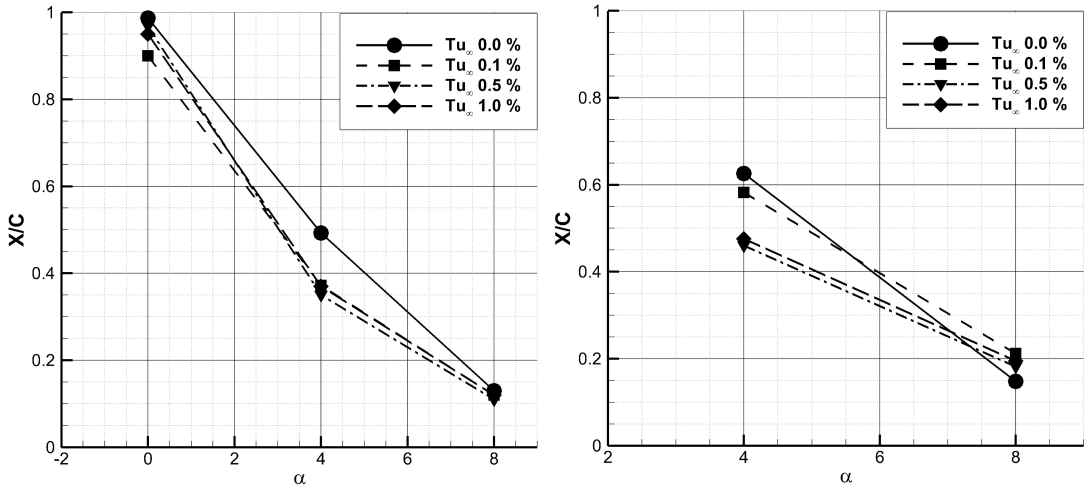

(a) Separation point

(b) Transition point

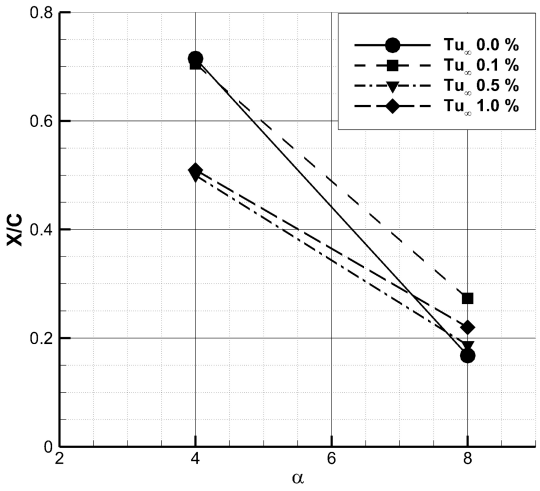

(c) Reattachment point

Fig. 5: LSB characteristics for SD 7003 airfoil at Re 6 $\times$ 10^4 using $k_T - k_L - \omega$ turbulence model

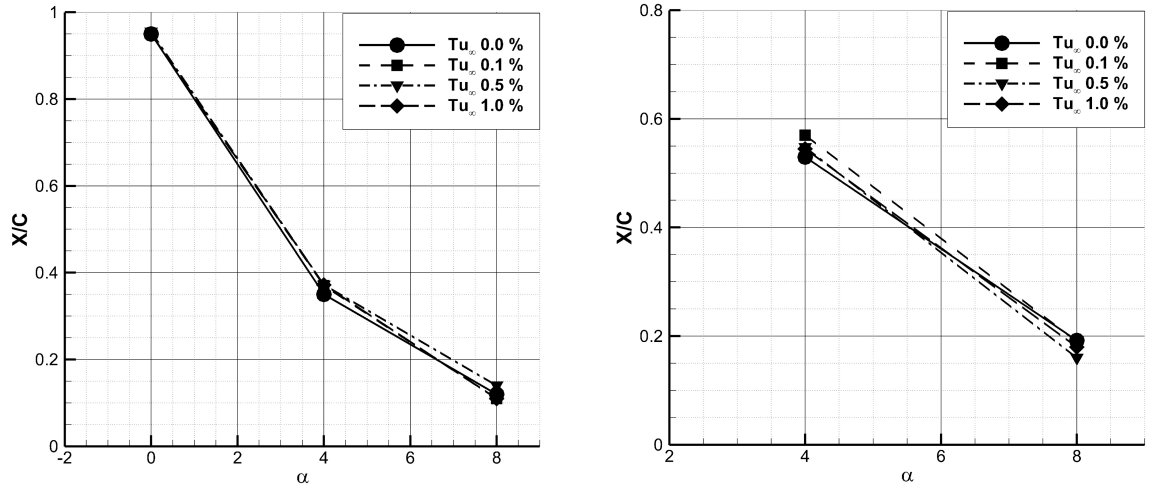

(a) Separation point

(b) Transition point

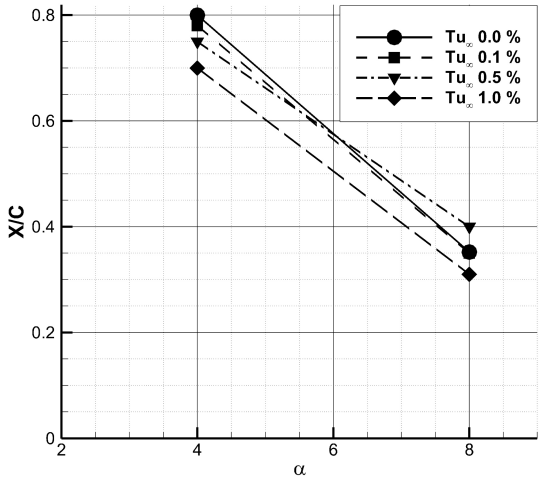

(c) Reattachment point

Fig. 6: LSB characteristics for SD 7003 airfoil at Re 6 $\times$ 10^4 using $k-\omega-SSTLM$ turbulence model

III. Results and discussion

The current section presents the time-averaged as well as instantaneous flow fields for the SD7003 airfoil at three Reynolds numbers and multiple turbulence intensities, using the physics and correlation-based turbulence models. The time-averaged results allow for careful side-by-side comparison of the near-wall flow physics resolved by the two turbulence models with varying flow angle of attack, turbulence intensity and Reynolds number. The instantaneous flow field analysis allows for attributing the near-wall physics to the time-varying aerodynamic characteristics such as

changes in C_l and C_d .

A. Mean characteristics

All simulations were run for a fixed time duration (5 seconds) using the variable time-step transient simulations, with an upper bound of 0.9 for the Courant number. Averaged flow-fields were computed by time-averaging the last 3 seconds of the simulation run time. An FFT analysis (not presented in this study) was conducted for the time-varying C_l for each case simulation and the solution was considered to have reached steady state or become periodic with time. Tables 2 and 3 list the mean LSB attributes with corresponding performance characteristics of the airfoil, for the $k_T - k_L - \omega$ and $k - \omega - SSTLM$ turbulence models, respectively. For the sake of brevity, measurements corresponding to only $Tu_\infty = 0.5\%$ are listed for moderate and high Reynolds numbers. Figures 7(a) and (b) illustrate the mean C_l characteristics for the SD7003 airfoil as a function of varying Tu_∞ and Fig. 7(c) represents the difference in C_l trends for varying turbulence models. Figure 7 indicates the $k - \omega - SSTLM$ turbulence model to be more sensitive to the changes in Tu_∞ as compared to the $k_T - k_L - \omega$ turbulence model.

Turbulence model	Reynolds Number	Tu(%)	α (^{o})	S_p (x/c)	T_p (x/c)	R_p (x/c)	C_l	C_d
$k_T - k_L - \omega$	0.6×10^5	0	0	0.987	-	-	0.043	0.013
$k_T - k_L - \omega$	0.6×10^5	0	4	0.493	0.626	0.715	0.528	0.025
$k_T - k_L - \omega$	0.6×10^5	0	8	0.13	0.148	0.168	0.790	0.051
$k_T - k_L - \omega$	0.6×10^5	0.1	0	0.901	-	-	0.041	0.014
$k_T - k_L - \omega$	0.6×10^5	0.1	4	0.372	0.582	0.705	0.519	0.033
$k_T - k_L - \omega$	0.6×10^5	0.1	8	0.12	0.212	0.791		0.057
$k_T - k_L - \omega$	0.6×10^5	0.5	0	0.968	-	-	0.043	0.013
$k_T - k_L - \omega$	0.6×10^5	0.5	4	0.350	0.461	0.505	0.525	0.024
$k_T - k_L - \omega$	0.6×10^5	0.5	8	0.112	0.182	0.187	0.792	0.056
$k_T - k_L - \omega$	0.6×10^5	1	0	0.951	-	-	0.043	0.013
$k_T - k_L - \omega$	0.6×10^5	1	4	0.371	0.476	0.510	0.528	0.025
$k_T - k_L - \omega$	0.6×10^5	1	8	0.121	0.195	0.221	0.771	0.055
$k_T - k_L - \omega$	0.6×10^6	0.5	0	0.950	-	-	0.170	0.006
$k_T - k_L - \omega$	0.6×10^6	0.5	4	0.251	0.261	0.272	0.609	0.008
$k_T - k_L - \omega$	0.6×10^6	0.5	8	0.111	0.135	0.14	0.940	0.025
$k_T - k_L - \omega$	0.6×10^7	0.5	0	0.953	-	-	0.174	0.007
$k_T - k_L - \omega$	0.6×10^7	0.5	4	0.04	0.051	0.08	0.605	0.010
$k_T - k_L - \omega$	0.6×10^7	0.5	8	0.018	0.02	0.03	0.979	0.016

Table 2: Simulation parameters for $k_T - k_L - \omega$ turbulence model

Turbulence model	Reynolds Number	Tu(%)	α (^{o})	S_p (x/c)	T_p (x/c)	R_p (x/c)	C_l	C_d
$k-\omega-SSTLM$	0.6×10^5	0	0	0.957	-	-	0.045	0.013
$k-\omega-SSTLM$	0.6×10^5	0	4	0.353	0.526	0.805	0.550	0.024
$k-\omega-SSTLM$	0.6×10^5	0	8	0.121	0.192	0.352	0.822	0.050
$k-\omega-SSTLM$	0.6×10^5	0.1	0	0.951	-	-	0.041	0.014
$k-\omega-SSTLM$	0.6×10^5	0.1	4	0.371	0.571	0.780	0.550	0.025
$k-\omega-SSTLM$	0.6×10^5	0.1	8	0.112	0.191	0.828		0.0489
$k-\omega-SSTLM$	0.6×10^5	0.5	0	0.955	-	-	0.044	0.014
$k-\omega-SSTLM$	0.6×10^5	0.5	4	0.372	0.548	0.75	0.558	0.025
$k-\omega-SSTLM$	0.6×10^5	0.5	8	0.111	0.192	0.351	0.828	0.048
$k-\omega-SSTLM$	0.6×10^5	1	0	0.950	-	-	0.045	0.013
$k-\omega-SSTLM$	0.6×10^5	1	4	0.372	0.476	0.700	0.548	0.024
$k-\omega-SSTLM$	0.6×10^5	1	8	0.110	0.186	0.311	0.835	0.0451
$k-\omega-SSTLM$	0.6×10^6	0.5	0	0.950	-	-	0.185	0.006
$k-\omega-SSTLM$	0.6×10^6	0.5	4	0.261	0.290	0.333	0.583	0.011
$k-\omega-SSTLM$	0.6×10^6	0.5	8	0.04	0.05	0.06	0.944	0.021
$k-\omega-SSTLM$	0.6×10^7	0.5	0	0.951	-	-	0.182	0.008
$k-\omega-SSTLM$	0.6×10^7	0.5	4	0.041	0.052	0.082	0.607	0.011
$k-\omega-SSTLM$	0.6×10^7	0.5	8	0.018	0.022	0.032	0.989	0.018

Table 3: Simulation parameters for $k-\omega-SSTLM$ turbulence model

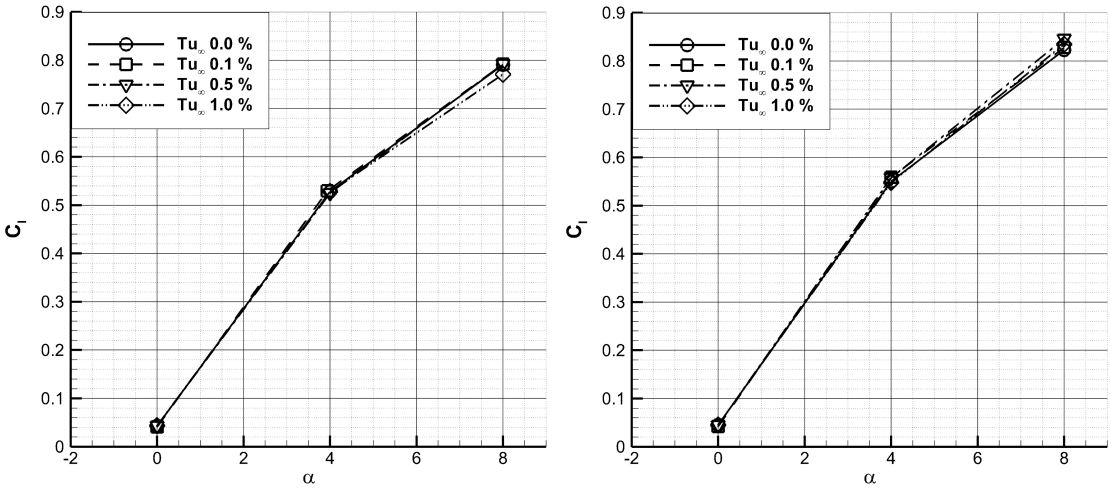

(a) $k_T - k_L - \omega$

(b) $k - \omega - SSTLM$

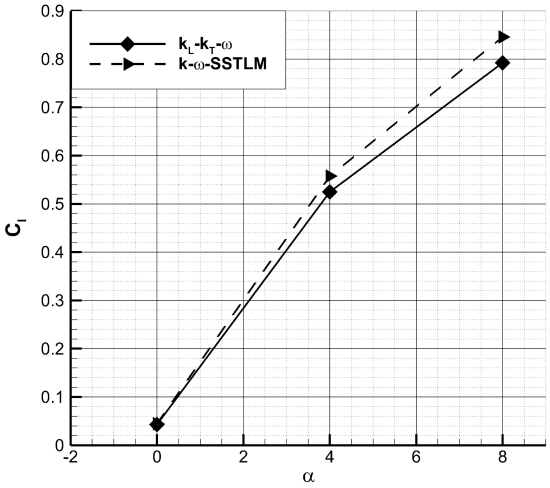

(c) C_l polar

Fig. 7: C_l characteristics for SD 7003 airfoil at Re 6 $\times$ 10^4

Fig. 8 represents the surface C_p distribution for SD7003 airfoil at multiple flow angles of attack (α) with Tu = 0 % and for Re 6 $\times$ 10^4. General trends from Figs. 8(a), (b) and (c) suggest an under-prediction of C_l for all three angles of attack. A key observation from Fig. 8 is the location and structure of the LSB. While no visible LSB structure is observed for the $\alpha = 0^0$ case, a clear separation, transition and reattachment point is seen for the remaining two cases. A distinguishing feature here is the structure of the LSB itself. For both the $\alpha = 4$ and $\alpha = 8$ cases, the physics based turbulence model results in a transition region characterized by small separation bubbles, whereas, on the other hand, the correlation based turbulence model predicts a large LSB structure

over the suction surface. A key observation here is the agreement of the onset of the transition region between the physics and correlation-based turbulence models. As expected, with an increase in α , the LSB size is observed to decrease and its location moves upstream towards the leading edge. At the same location of transition as that predicted by the correlation-based model, the C_p distribution from the physics-based turbulence model indicates multiple peaks, thus suggesting LSB breakdown to smaller structures.

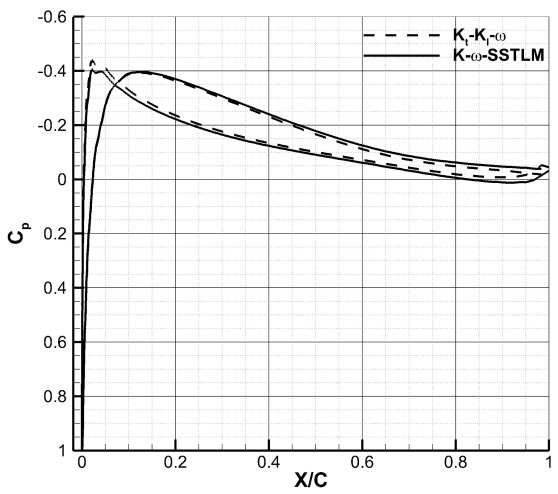

(a) $\alpha = 0^0$

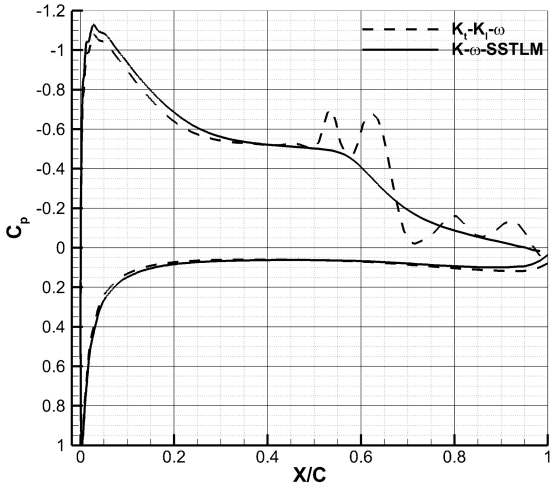

(b) $\alpha = 4^0$

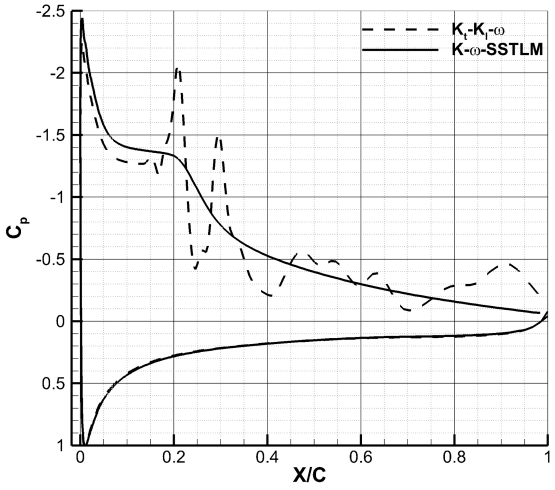

(c) $\alpha = 8^0$

Fig. 8: Surface C_p distribution for the SD 7003 airfoil at Re 6 $\times$ 10^4, Tu = 0 %.

Figure 9 represents the mean surface distribution for the SD7003 airfoil at Re 6 $\times$ 10^4 and Tu = 0.1 %. The overall trends observed here are similar to those in Fig. 8 except for the case of the

physics-based turbulence model at $\alpha = 8^0$, wherein the LSB structure is now observed to undergo breakdown into smaller regions of re-circulation, post transition. Another observation critical to the low-Reynolds number prediction capability of the two models is the relatively larger disagreement in the surface pressure distribution between the physics and correlation-based models, in the region $0.05 < X/C < 0.2$, as observed in Fig. 9.

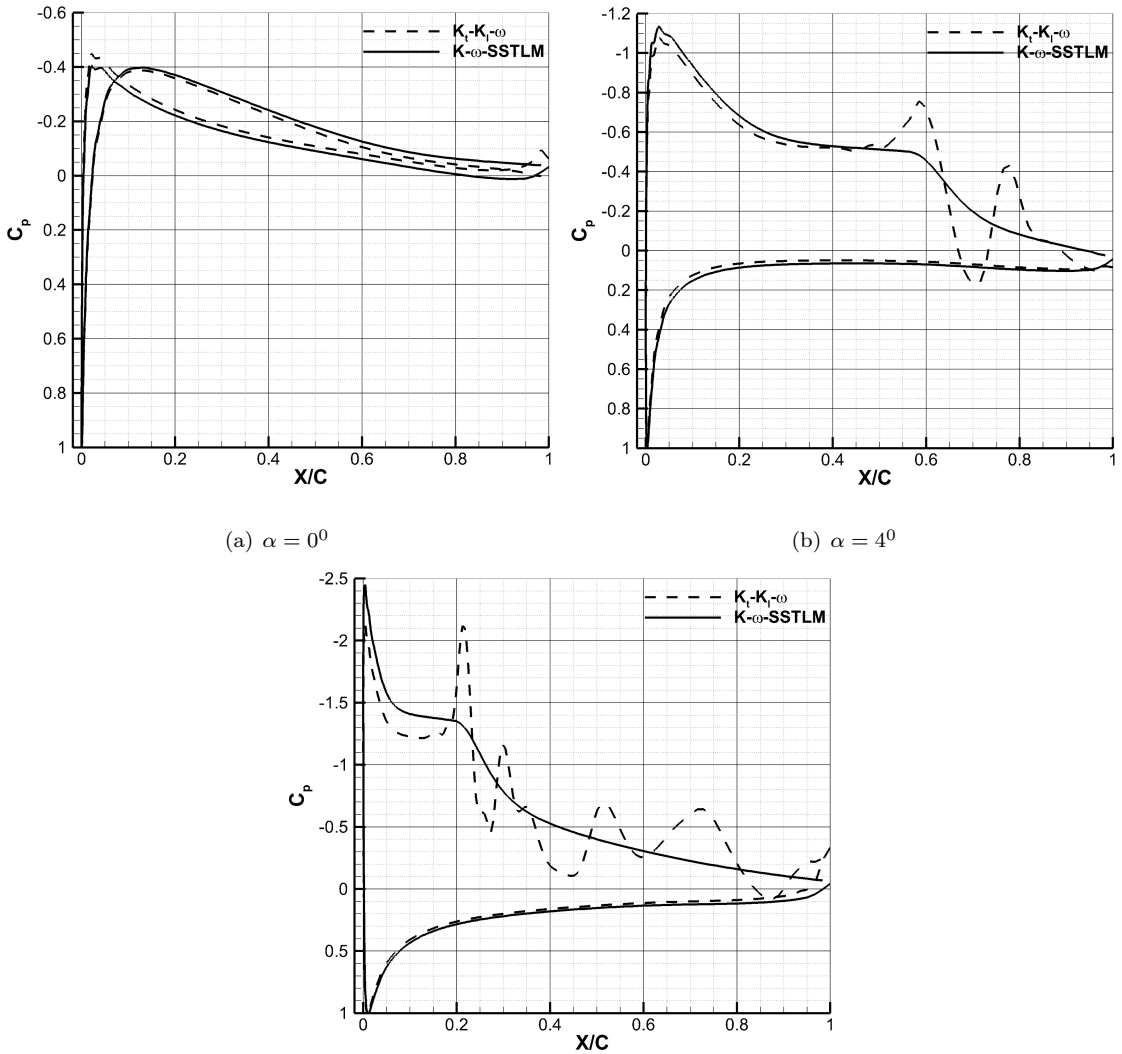

(a) $\alpha = 0^0$

(b) $\alpha = 4^0$

(c) $\alpha = 8^0$

Fig. 9: Surface C_p distribution for SD 7003 airfoil at Re 6 $\times$ 10^4, Tu = 0.1 %.

Figures. 10 and 11 represent the time-averaged surface C_p distributions for the SD7003 airfoil at Re 6 $\times$ 10^4 with Tu = 0.5 % and Tu = 1 %, respectively. For $\alpha = 0^0$, with an increase in free-stream turbulence intensity, a LSB structure is observed for the physics-based turbulence model case.

Careful comparison for of Figs. 9(b), 10(b) and 11(b) suggests an increase in smaller separation structures in the pre-transition region. For the $\alpha = 8^0$ case, an increase in the number of re-circulation structures is observed with the increase in free-stream turbulence intensity. Another key difference observed here is the delayed onset of transition predicted by the physics-based turbulence model with the increase in free-stream turbulence.

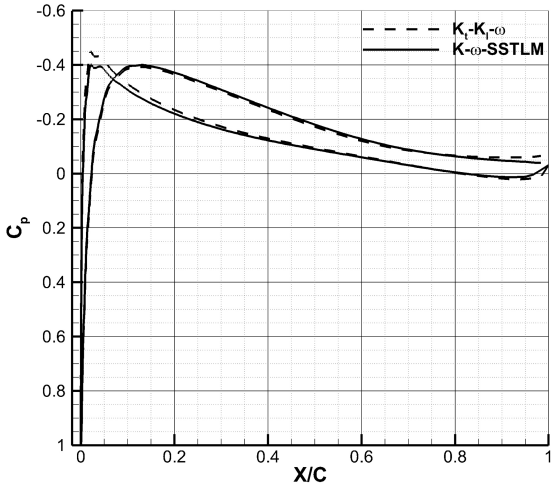

(a) $\alpha = 0^0$

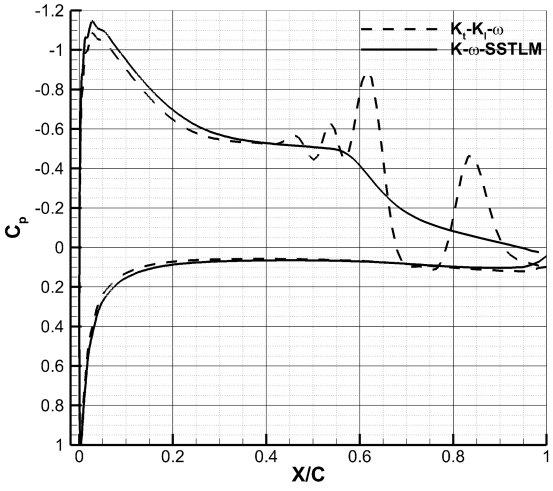

(b) $\alpha = 4^0$

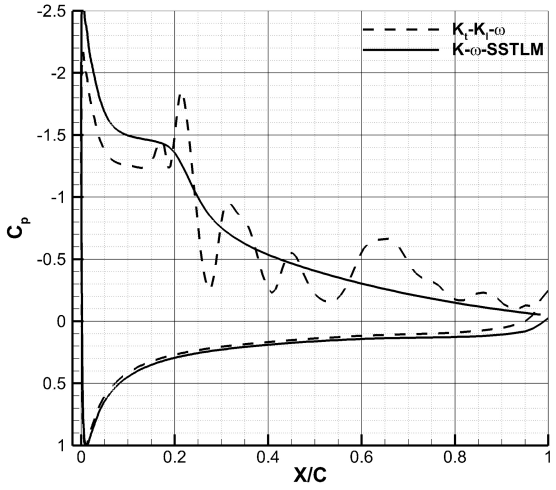

(c) $\alpha = 8^0$

Fig. 10: Surface C_p distribution for the SD 7003 airfoil at Re 6 $\times$ 10^4, Tu = 0.5 %.

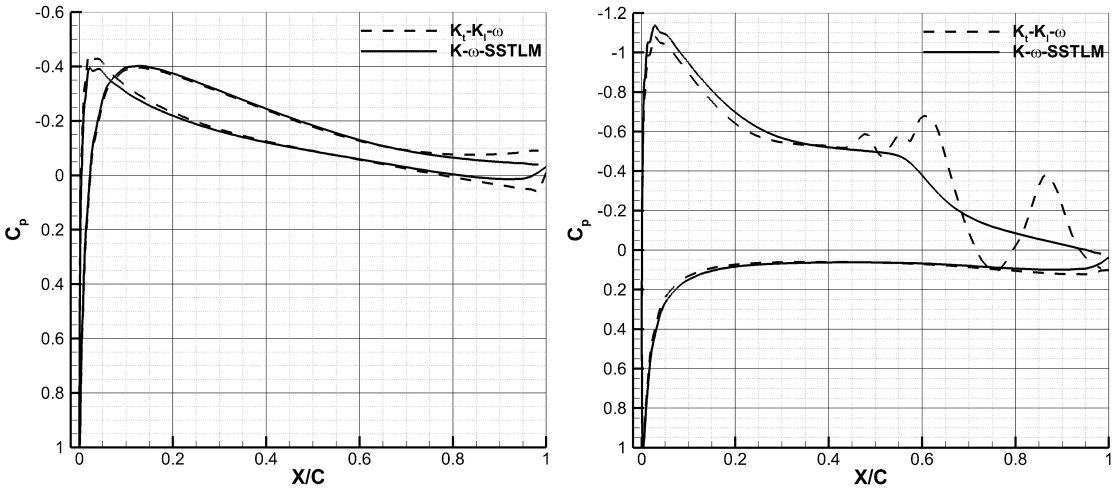

(a) $\alpha = 0^0$

(b) $\alpha = 4^0$

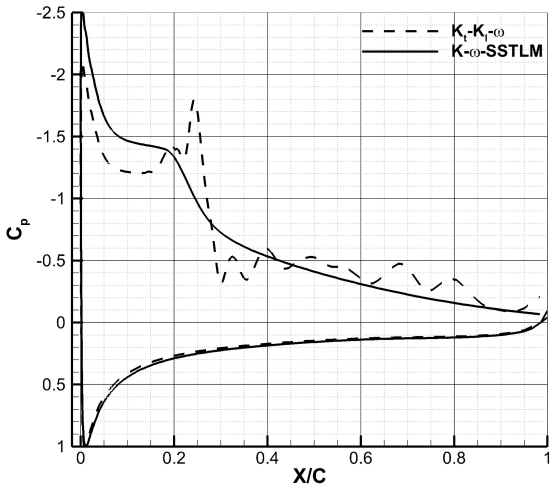

(c) $\alpha = 8^0$

Fig. 11: Surface C_p distribution for the SD 7003 airfoil at Re 6×10^4, Tu = 1 %.

The effects of increasing free-stream turbulence intensity can also be observed in Figs. 12 and 13 wherein the surface C_p distribution for the SD 7003 airfoil at Re 6×10^4 is shown for increasing Tu_∞. As observed earlier, an increase in Tu_∞ results in relatively early onset of transition for the physics-based turbulence model. The correlation-based turbulence model on the other hand is observed to be relatively less sensitive to free-stream turbulence characteristics.

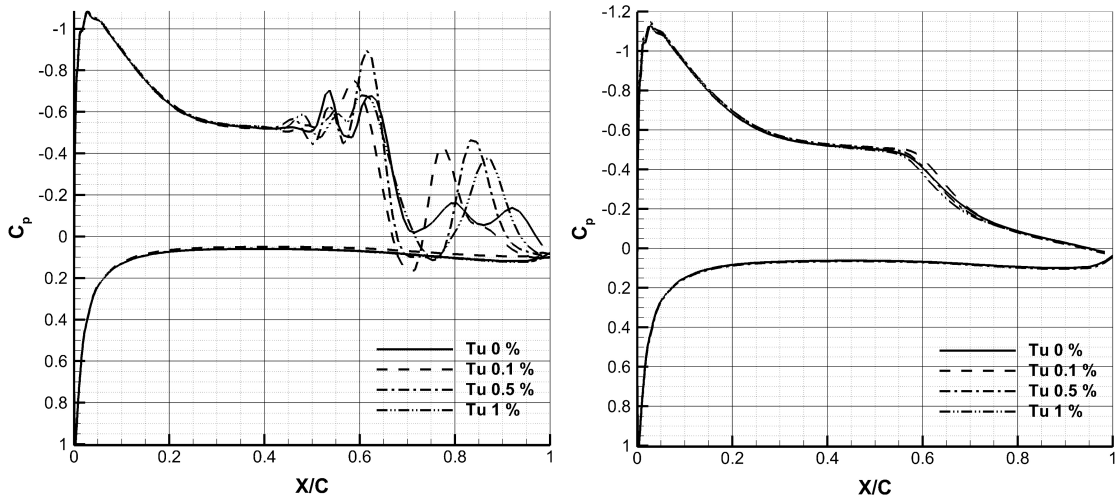

(a) $k_T - k_L - \omega$ (b) $k - \omega - SSTLM$

Fig. 12: Surface C_p distribution for the SD 7003 airfoil at Re 6 $\times$ 10^4 with multiple free-stream turbulence intensities.

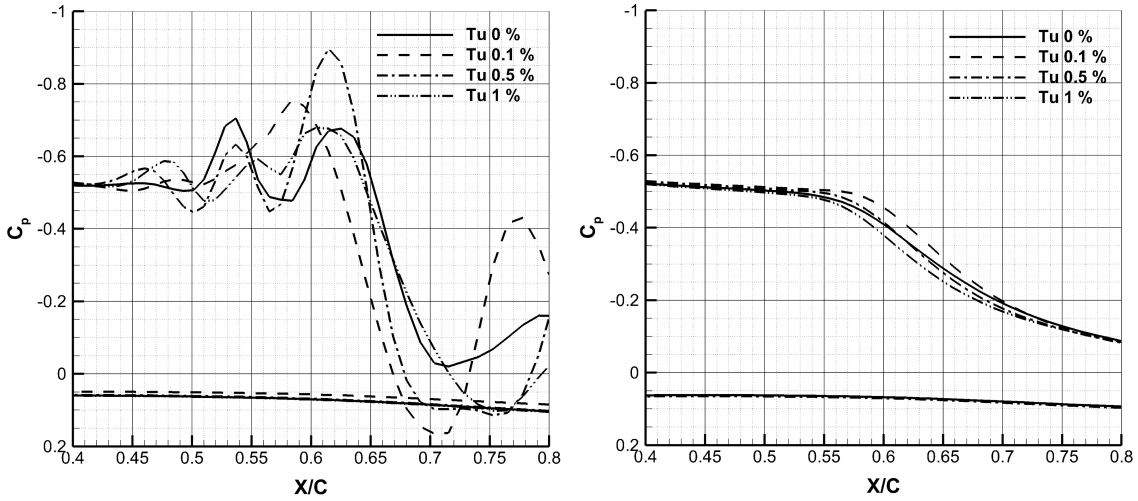

(a) $k_T - k_L - \omega$ (b) $k - \omega - SSTLM$

Fig. 13: Surface C_p distribution for the SD 7003 airfoil at Re 6 $\times$ 10^4 with multiple free-stream turbulence intensities.

Fig. 14 illustrates the surface C_p distribution for the SD7003 airfoil at low, moderate and high Reynolds numbers, with prescribed $Tu_\infty = 0.5$ %. Similar to the observations made in previous studies [10, 11, 13, 30], an increase in Reynolds number leads to a decrease in LSB size. As seen

earlier, for a low Reynolds number of Re 6×10^4, both turbulence models predict the onset of transition with reasonable agreement with one another. For moderate and high Reynolds numbers, an increase in C_l is is observed for both models along with a small LSB structure, located upstream towards the leading edge.

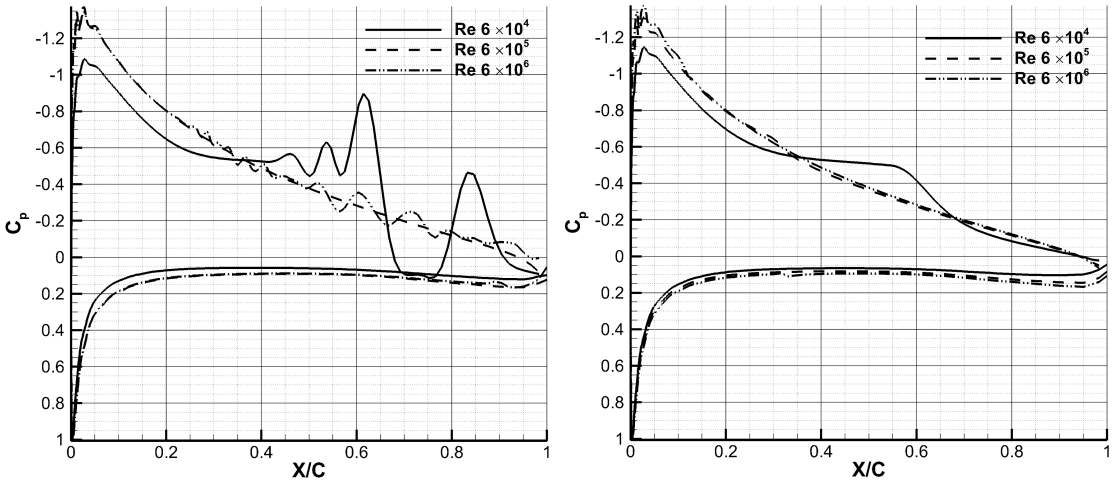

(a) $k_T - k_L - \omega$ (b) $k - \omega - SSTLM$

Fig. 14: Surface C_p distribution for the SD 7003 airfoil at multiple Reynolds numbers and $Tu_\infty = 0.5\%$

IV. Instantaneous characteristics

Instantaneous flow-field characteristics in the near-wall region allow for clear illustration of LSB prediction capability of the two turbulence models. Instantaneous flow attributes are shown only for Re_c 6×10^4 since well-resolved instantaneous features are extracted at this flow regime. Figures 15 and 16 illustrate the velocity vectors and separation region contours in the trailing edge region, using the two turbulence models, at an instance of maximum C_l. No LSB structure is observed for the two turbulence models at either $Tu_\infty = 0\%$ or $Tu_\infty = 1\%$. Instead, the re-circulation region is observed to oscillate between the upper and lower surface, thus violating the Kutta condition. This observation is consistent with the mean trends of C_p distribution seen earlier in Figs. 8 and 11, wherein the flow is observed to detach at the trailing edge. This observation was found to be synonymous to that of [15], for a NACA0012 airfoil configuration , subjected to a similar flow regime. Another key observation is the effect of Tu_∞ on the size and length of the separation region.

With an increase in Tu_∞ from 0 to 1%, the length of the separation region is seen to increase.

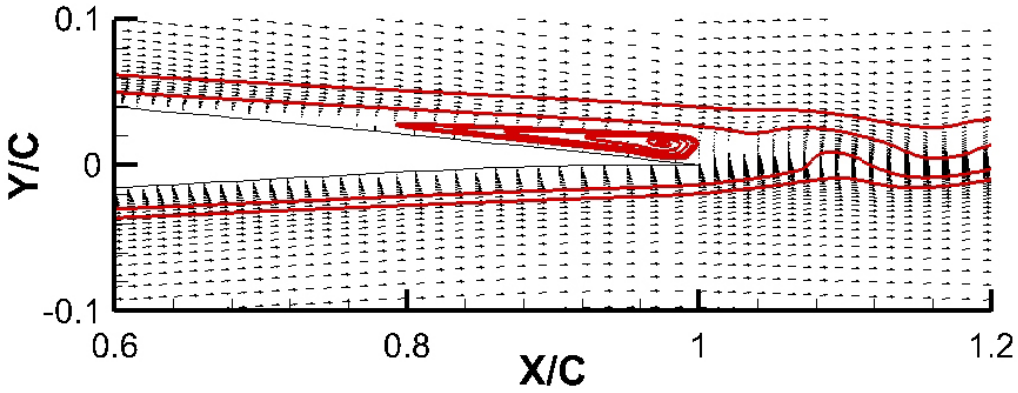

(a) $k_T - k_L - \omega$

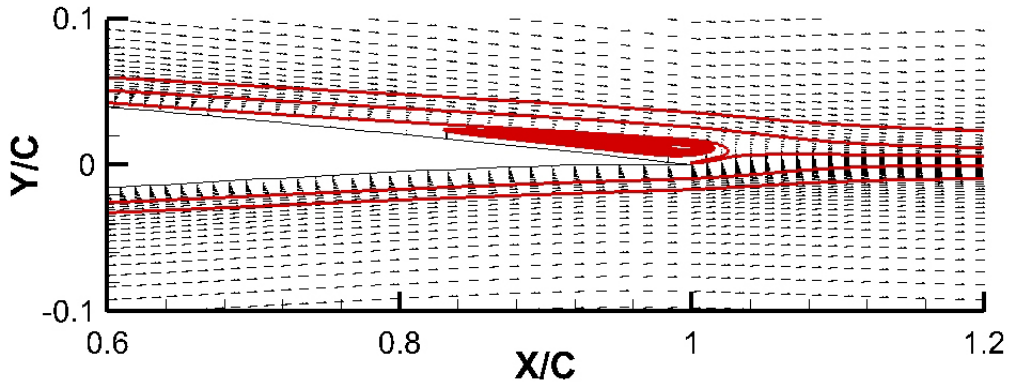

(b) $k - \omega - SSTLM$

Fig. 15: Instantaneous flow separation characteristics at trailing edge at Re 6×10^4, $\alpha = 0^0$ and $Tu_\infty = 0\%$

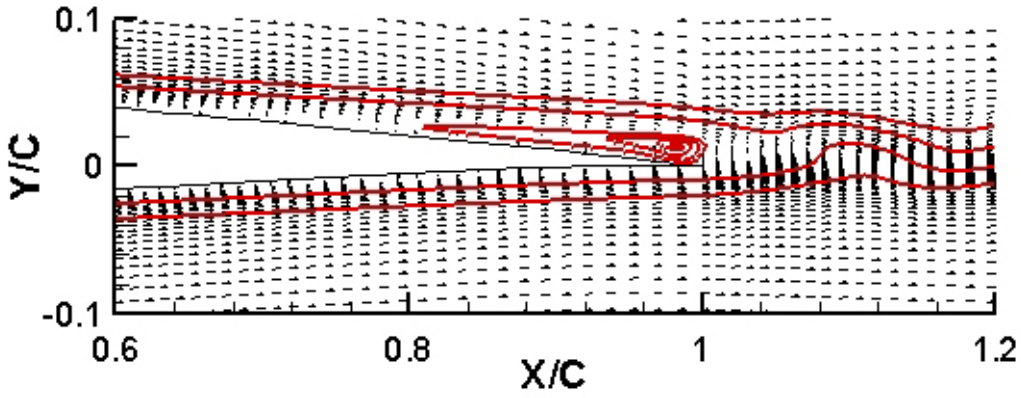

(a) $k_T - k_L - \omega$

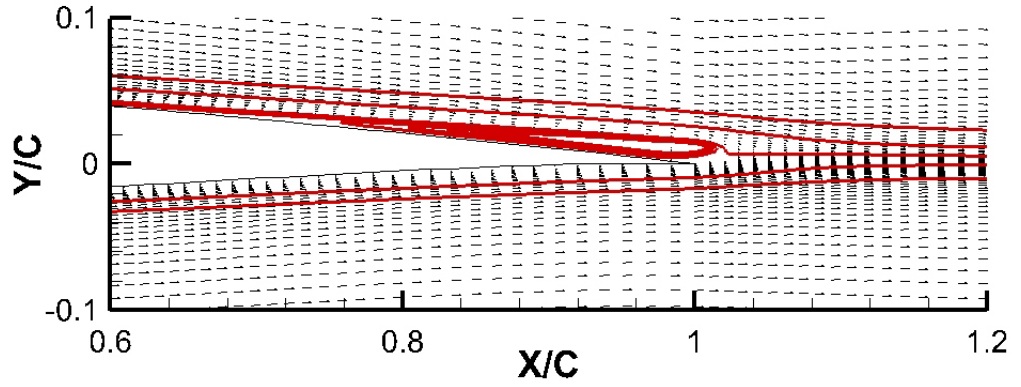

(b) $k - \omega - SSTLM$

Fig. 16: Instantaneous flow separation characteristics at trailing edge at Re 6×10^4, $\alpha = 0^0$ and $Tu_\infty = 1\%$

Figures 17 and 18 represent the near-wall LSB characteristics for the SD 7003 airfoil, subjected to flow at $\alpha = 4^0$ and $Tu_\infty = 0$ %, at instances of both maximum and minimum C_l. At maximum C_l (Fig. 17(a)), a primary vortex is shed from the LSB and the re-attachment point moves upstream towards the leading edge. At minimum C_l, the LSB sheds a secondary and tertiary vortex that move upstream towards the leading edge, and a primary vortex that moves the re-attachment point downstream towards the trailing edge. With an increase in Tu_∞, the length of the LSB is seen to increase in general, however the primary vortex shed from the LSB is now relatively upstream for the minimum C_l case when compared for the $Tu_\infty = 0\%$ case.

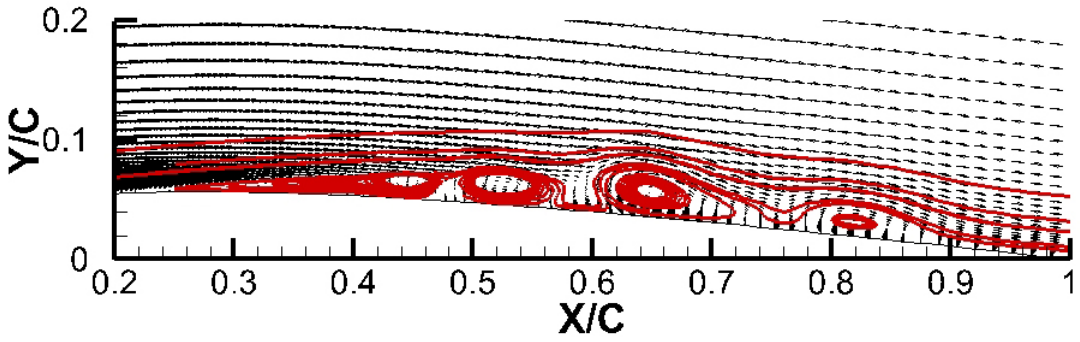

(a) Max C_l

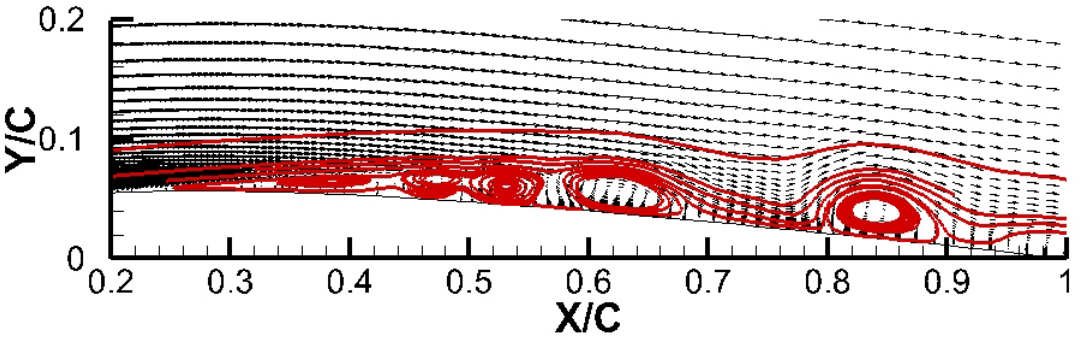

(b) Min C_l

Fig. 17: Near-wall flow characteristics at Re 6×10^4, $\alpha = 4^0$ and $Tu_\infty = 0\%$, using $k_L - k_T - \omega$ turbulence model

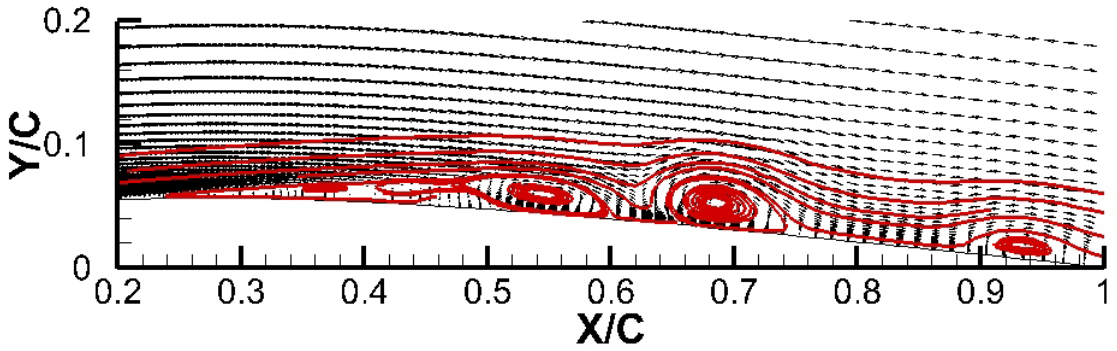

(a) Max C_l

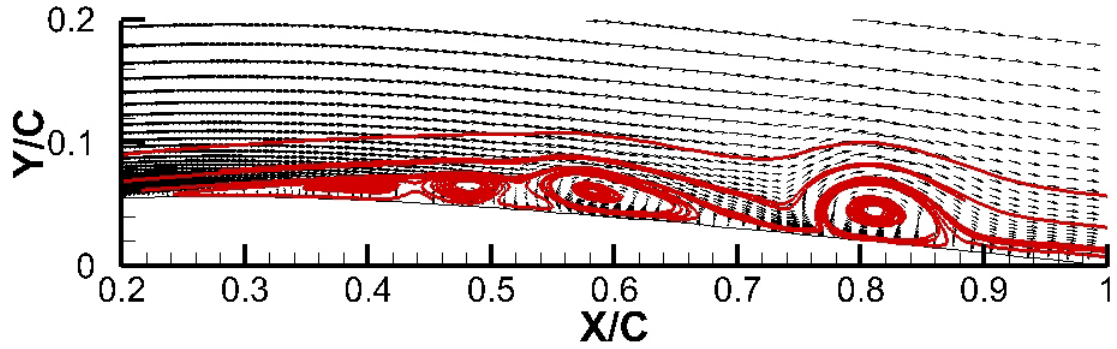

(b) Min C_l

Fig. 18: Near-wall flow characteristics at Re 6×10^4, $\alpha = 4^0$ and $Tu_\infty = 1\%$, using $k_L - k_T - \omega$ turbulence model

Figures 19 and 20 indicate no key differences in the LSB structure for the correlation based turbulence model at instances of maximum and minimum C_l. However with increasing Tu_∞, the LSB length is observed to decrease and the LSB is seen to move upstream, thus indicating an increase in C_l. The general structure of the LSB is found to be in agreement with the C_p trends seen earlier in Figs. 8 and 11 and literature [37], wherein a long and stable bubble over the suction surface is observed. As observed, the LSB sheds no vortices unlike the case of the physics-based turbulence model, hence the smooth plateau observed in previous section.

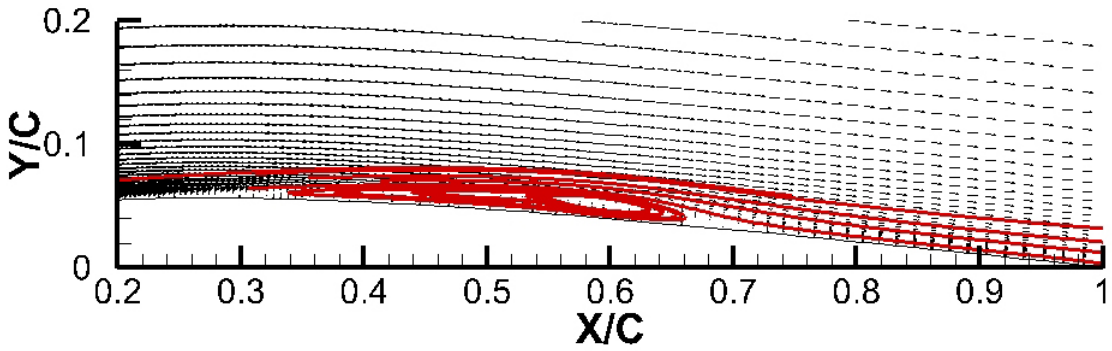

(a) Max C_l

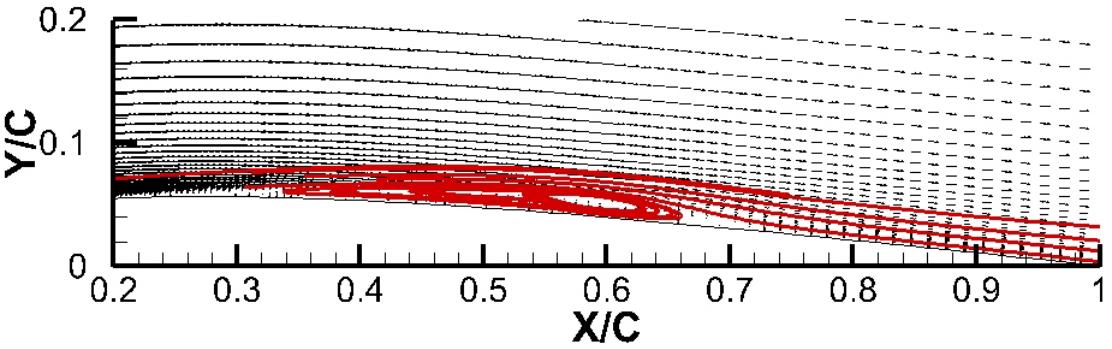

(b) Min C_l

Fig. 19: Near-wall flow characteristics at Re 6×10^4, $\alpha = 4^0$ and $Tu_\infty = 0.1\%$, using $k-\omega-SSTLM$ turbulence model

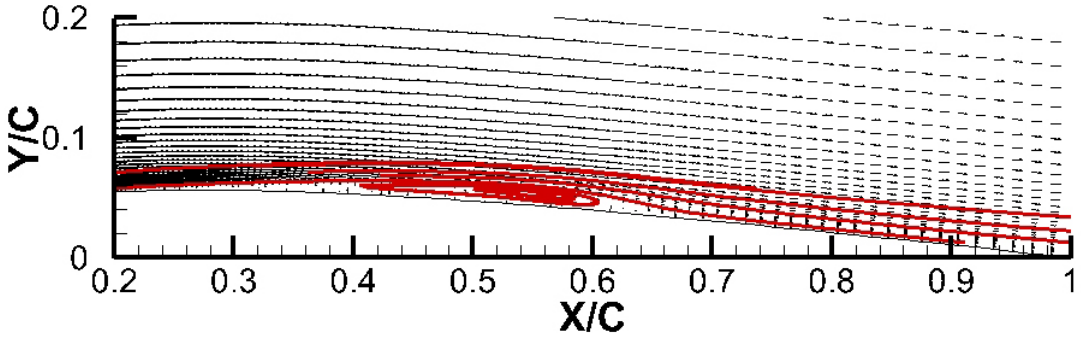

(a) Max C_l

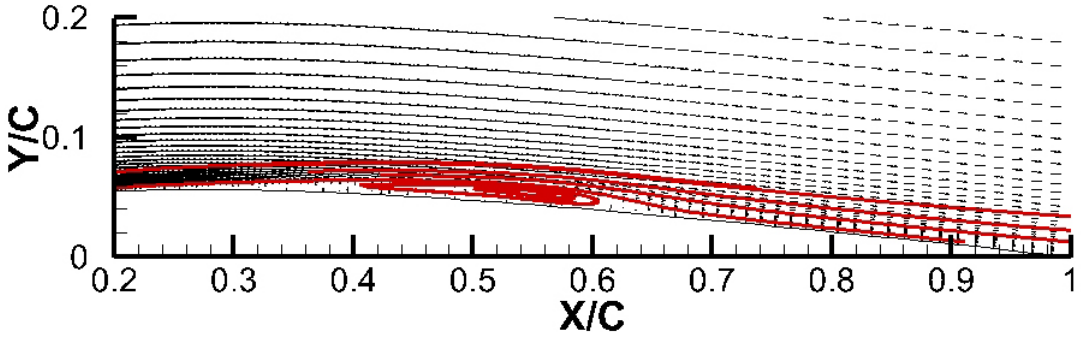

(b) Min C_l

Fig. 20: Instantaneous flow separation characteristics at trailing edge at Re 6×10^4, $\alpha = 4^0$ and $Tu_\infty = 1\%$

V. Conclusions

Extensive three-dimensional URANS simulations to understand the application of a physics and correlation-based turbulence models were conducted wherein the effect of Tu_∞, α and Re_c on the onset of flow transition and LSB characteristics were studied. The solution accuracy was determined for both the models using reference surface pressure measurements obtained from an Implicit Large Eddy Simulation, available in the literature. While both turbulence models predict the onset of flow transition, a relatively stable LSB structure is observed using the $k-\omega-SSTLM$ turbulence model. Design of a *Naturally Laminar Flow* airfoil requires accurate prediction of transition location and then varying the outer mold line such that the onset point is further downstream near the trailing edge. The simulation procedure employed in the current study, especially using the $k-\omega-SSTLM$

turbulence model, can be used as a part of an airfoil design optimization routine wherein the distance between the leading edge and the transition onset point is maximized. From a pure physics perspective, this study can be extended to three-dimensional lifting surfaces wherein the effect of span-wise cross-flow on flow transition attributes are also examined.

References

[1] Wright, W., "The Wright Brothers Aeroplane," *The Aeronautical Journal*, 20(79), 100-106, 1916.

[2] Anderson, K. and Gaston, K.J., "Lightweight unmanned aerial vehicles will revolutionize spatial ecology, " *Frontiers in Ecology and Environment*, Vol 11, No 3, pp. 138-146, 2013

[3] Pajares, G., "Overview and current status of remote sensing applications based on unmanned aerial vehicles (UAVs) ," *Photogrammetric Engineering & Remote Sensing*, Vol 81, No 4, pp. 281-330, 2015

[4] Valavanis, K.P., "Advances in unmanned aerial vehicles: state of the art and the road to autonomy," *Springer Science & Business Media*, Vol 33, 2008

[5] Hardin, P.J. and jensen, R.R., "Small-scale unmanned aerial vehicles in environmental remote sensing: Challenges and opportunities," *GIScience & Remote Sensing*, Vol 48, No 1, pp. 99-111, 2011

[6] Everaerts, J., " The use of unmanned aerial vehicles (UAVs) for remote sensing and mapping, " *The International Archives of the Photogrammetry, Remote Sensing and Spatial Information Sciences*, Vol 37, pp. 1187-1192, 2008

[7] Grossman, B., Gurdal, Z., Haftka, R.T., Straunch, G.J. and Eppard, W.M., " Integrated aerodynamic/structural design of a sailplane wing, " *Journal of Aircraft*, Vol 25, No 9, pp. 855-860, 1988

[8] Maughmer, M., " The Evolution of Sailplane Wing Design, " *In AIAA International Air and Space Symposium and Exposition: The Next 100 Years*, p. 2777, 2003.

[9] Catalano, P. and Tognaccini, R., " Turbulence Modeling for Low-Reynolds-Number Flows, " *AIAA Journal*, Vol. 48, No. 8, pp. 1673-1685, 2010

[10] O'meara, M. and Mueller, T.J., " Laminar separation bubble characteristics on an airfoil at low Reynolds numbers, " *AIAA Journal*, Vol. 25, NO. 8, pp. 1033-1041, 1987

[11] Theofilis, V., Hein, S. and Dallmann, U., " On the origins of unsteadiness and three-dimensionality in a laminar separation bubble, " *Philosophical Transactions of the Royal Society of London A: Mathematical, Physical and Engineering Sciences*, Vol. 358, No. 1777, pp. 3229-3246, 2000

[12] Alam, M. and Sandham, N.D., "Direct numerical simulation of short laminar separation bubbles with turbulent reattachment, " *Journal of Fluid Mechanics*, Vol. 410, pp. 1-28, 2000

[13] Hain, R., KÃďhler, C.J. and Radespiel, R., " Dynamics of laminar separation bubbles at Low-Reynolds-number aerofoils, " *Journal of Fluid Mechanics*, Vol. 630, pp. 129-153, 2009

[14] Burgmann, S., BrÃijcker, C. and SchrÃűder, W., "Scanning PIV measurements of a laminar separation bubble, " *Experiments in Fluids*, Vol. 41, No. 2, pp. 319-326, 2006

[15] Counsil, J.N.N and Boulama, K.G., "Low-Reynolds-Number Aerodynamic Performances of the NACA 0012 and Selig-Donovan 7003 Airfoils," *Journal of Aircraft*, Vol. 50, No. 1, pp. 204-2015, 2013

[16] Drela, M., " Improvements in Low Reynolds Number Airfoil Flow Predictions with ISES and XFOIL, " *Massachusetts Inst. of Technology CFl Rept. 91-5*, Cambridge, MA, 1991

[17] Radespiel, R., Graage, K. and Brodersen, O., "Transition Predictions Using Reynolds-Averaged navier-Stokes and Linear Stability Analysis Methods, " *AIAA Paper 91-1641*, 1991

[18] Shur, M., Spalart, P.R., Strelets, M. and Travin, A., "Detached-eddy simulation of an airfoil at high angle of attack, " *In Engineering Turbulence Modeling and Experiments*, Vol. 4, pp. 659-678, 1999

[19] Wang, Z.J., Fidkowski, K., Abgrall, R., Bassi, F., Caraeni, D., Cary, A., Deconinck, H., Hartmann, R., Hillewaert, K., Huynh, H.T. and Kroll, N., "High-order CFD methods: current status and perspective," *International Journal for Numerical Methods in Fluids*, Vol 72, No. 8, pp. 811-845, 2013

[20] Ranjan, P. and Ansell, P.J.,"Computational Analysis of Vortex Wakes Without Near-Field Rollup Characteristics, " *Journal of Aircraft* , pp.1-14, 2018

[21] Ranjan, P., Ansell, P.J. and James, K.A.," Optimal Hyperelliptic Cambered Span Configurations for Minimum Drag, " *Journal of Aircraft* , pp.1-13, 2018

[22] Howard, R.J.A., Alam, M. and Sandham, N.D., "Two-equation turbulence modeling of a transitional separation bubble, " *Flow, turbulence and combustion*, Vol. 63, No 4, pp. 175-191, 2000

[23] Benton, J., Kalitzin, G. and Gould, A., "Application of two-equation turbulence models in aircraft design, " *In 34th Aerospace Sciences Meeting and Exhibit*, p. 327, 1996

[24] Ducros, F., Comte, P. and Lesieur, M., "Large-eddy simulation of transition to turbulence in a boundary layer developing spatially over a flat plate, " *Journal of Fluid Mechanics*, Vol. 326, pp. 1-36, 1996

[25] Lien, F.S., Kalitzin, G. and Durbin, P.A., "RANS modeling for compressible and transitional flows, " *Proceedings of the Stanford University Center for Turbulence Research Summer Program*, pp. 267-286, 1998

[26] Menter, F.R., Esch, T. and Kubacki, S., "Transition modeling based on local variables, " *In Engineering Turbulence Modeling and Experiments*, Vol. 5, pp. 555-564, 2002

[27] Wilcox, D.C., " Turbulence Modeling for CFD, " *DCW Industries, Los Angeles, CA*, 1994

[28] Menter, F.R., " Two-Equation Eddy Viscosity Turbulence Models for Engineering Applications, " *AIAA*

Journal, Vol. 32, No. 8, pp. 1598-1695, 1994

[29] Wallin, S., and Johansson, A., " An Explicit Algebraic Reynolds Stress Model for Incompressible and Compressible Turbulent Flows, " *Journal of Fluid Mechanics*, Vol. 403, pp. 89-132, 2000

[30] Galbraith, M.C., and Visbal, M.R., "Implicit Large Eddy Simulation of Low Reynolds Number flow past the SD 7003 Airfoil ," *46th AIAA Aerospace Sciences Meeting and Exhibit, AIAA paper 225*, 2008

[31] Catalano, P. and Tognaccini, R., "Turbulence Modeling for Low-Reynolds-Number Flows, " *AIAA Journal*, Vol. 48, No. 8, pp. 1673-1685

[32] Langtry, R.B., and Menter, F.R., " Correlation-Based Transition Modeling for Unstructured Parallelized Computational Fluid Dynamics Codes, " *AIAA Journal*, Vol. 47, No. 12, pp. 2894-2906, 2009

[33] Walters, D.K. and Cokljat, D., " A Three-Equation Eddy-Viscosity Model for Reynolds-Averaged Navier-Stokes Simulations of Transitional Flow, " *Journal of Fluids Engineering*, Vol. 130, No. 12, 121401, 2008

[34] Rosetti, G.F., Vaz, G. and Fujarra, A.L., "URANS calculations for smooth circular cylinder flow in a wide range of Reynolds numbers: solution verification and validation, " *Journal of Fluids Engineering*, Vol. 134, No. 12, p.121103

[35] Bernardini, C., Carnevale, M., Manna, M., Martelli, F., Simoni, D. and Zunino, "Turbine blade boundary layer separation suppression via synthetic jet: An experimental and numerical study , " *Journal of thermal science*, Vol. 21, No. 5, pp. 404-412

[36] Tucker, P.G., "Unsteady computational fluid dynamics in aeronautics, " *Springer Science & Business Media*, Vol. 104, 2013

[37] Ol., M.V., McAuliffe, B.R., Hanff, E.S., Scholz, U., Kahler, C., " Comparison of Laminar Separation Bubble Measurements on a Low Reynolds Number Airfoil in Three Facilities, " *In 35th AIAA Fluid Dynamics Conference and Exhibit, AIAA paper 5149*, 2005

[38] Jones, L.E., Sandberg, R.D. and Sandham, N.D., " Direct Numerical Simulations of Forced and Unforced Separation Bubbles on an Airfoil at Incidence, " *Journal of Fluid Mechanics*, Vol. 602, pp. 175-207, 2008

[39] Kim, D.H., Yang, J.H., Chang, J.W., and Chung, J., " Boundary Layer and Near-Wake Measurements of NACA 0012 Airfoil at low Reynolds Numbers, " *AIAA Aerospace Sciences Meeting including the New Horizons Forum and Aerospace Exposition, Orlando, FL*, 2009

[40] Wahidi, R. and Bridges, D., "Experimental Investigation of the Boundary Layer and Pressure Measurements on Airfoils with Laminar Separation Bubbles," *AIAA Fluid Dynamics Conference, San Antonio, TX*, 2009

[41] Selig, M.S., Guglielme, J.J., Broeren, A.P., and Giguere, P., " Summary of Low-Speed Airfoil Data, " *Soartech publications*, Vol. 1, 1995

[42] Weller, H.G., Tabor, G., jasak, H., and Fureby, C., "A Tensorial Approach to Computational Continuum Mechanics Using Object-Oriented Technique, " *Computers in Physics*, Vol. 12, No. 6, p. 620, 1998.

[43] Forde, B.W., Foschi, R. O., and Stiemer, S. F., " Object-Oriented Finite Element Analysis, " *Computers and Structures*, Vol. 34, No. 3, pp. 355-374, 1990

[44] Doolan, C., " Flow and Noise Simulation of the NASA Tandem Cylinder Experiment Using OpenFOAM, " *In 15th AIAA/CEAS Aeroacoustics Conference, AIAA Paper 3157*, 2009

[45] Balogh, M., Parente, A., and Benocci, C., " RANS Simulation of ABL Flow over Complex Terrains Applying an Enhanced kâĂŞEpsilon Model and Wall Function Formulation: Implementation and Comparison for Fluent and OpenFOAM, " *Journal of Wind Engineering and Industrial Aerodynamics*, Vol. 104, pp. 360-368, 2012

[46] Muntean, S., Nilsson, H., and Susan-Resiga, R. F., " 3D Numerical Analysis of the Unsteady Turbulent Swirling Flow in a Conical Diffuser Using Fluent and OpenFOAM, " *Proceedings of the 3rd IAHR International Meeting of the Workgroup on Cavitation and Dynamic Problems in Hydraulic Machinery and Systems, Brno Univ. of Technology, Brno, Czech Republic*, pp. 14-16, 2009

[47] Mack, A., and Spruijt, M. P. N., " Validation of OpenFoam for Heavy Gas Dispersion Applications, " *Journal of Hazardous Materials*, Vol. 262, pp. 504-516, 2013

[48] Liu, Q., Gomez, F., Perez, J. M., and Theofilis, V., " Instability and Sensitivity Analysis of Flows Using OpenFOAM, " *Chinese Journal of Aeronautics*, Vol. 29, No. 2, pp. 316-325, 2016

[49] Furst, J, "Numerical simulation of transitional flows with laminar kinetic energy, " *Engineering Mechanics*, Vol. 20, No. 5, pp. 379-388, 2013.

[50] MATLAB:2010, "Version 7.10.0 (R2010a), " *The Mathworks Inc.*, Natick, Massachusetts, 2010.